ANALYSIS OF AIR BUBBLES PROBABILITY DISTRIBUTION FUNCTIONS IN A LARGE-SIZE DROPSHAFT

Carlo Gualtieri[1] - Hubert Chanson[2]

[1] Hydraulic and Environmental Engineering Department *Girolamo Ippolito*, University of Napoli *Federico II*, Napoli, Italy - E-mail: carlo.gualtieri@unina.it
[2] Department of Civil Engineering, The University of Queensland, Brisbane QLD 4072, Australia - E-mail: h.chanson@uq.edu.au

ABSTRACT

Dropshafts are commonly used in sewers and stormwater channels as energy dissipator systems. Since recent effort has been devoted to characterize dropshaft hydraulics and air-water flow properties, and the present paper develops an analysis of the bubbles probability distribution functions (PDF) in a shaft pool using new experiments conducted in a large-size facility. First, theoretical trajectory calculations of the free-falling nappe were compared with the maximum void fraction data observed within the pool. Then, statistical analysis was performed on both air and water chord length data. PDF was derived as well as mean, median, mode, standard deviation, skewness and kurtosis values. Further, these results were compared with some earlier work. The results obtained over the pool length at various vertical elevation highlighted some new insights on the interactions between turbulence, bubble coalescence and detrainment of the air bubbles.

1 FOREWORD

A dropshaft is an energy dissipator connecting two channels with different invert elevations. This type of structure is commonly used in sewers [1] and storm water systems. Small dropshafts are also used upstream and downstream of culverts [2], while large spillway shafts were built [3]. The dropshaft is an ancient design since Roman aqueducts [4] but there is however some controversy if it was used only for energy dissipation or also for flow re-aeration. Despite such long usage, the hydraulics of dropshafts has not been systematically documented [1] [2] [5]. Recent works [4] [6] [7] studied the hydraulics including the air-water flow properties.

This paper presents new experiments conducted in a large-size rectangular dropshaft located at the University of Queensland (Australia). It is focused on the analysis of probability distribution functions of air bubbles over the pool height at different depths below the free surface. The PDFs were compared with earlier works obtained for different flow rates and the results highlight some new insights on the interactions between turbulence, bubble coalescence and detrainment of the bubbles.

2 EXPERIMENTAL SETUP

The experiments herein described were performed in a large-size rectangular dropshaft built in marine plywood and perspex at the Hydraulics Laboratory at the University of Queensland (Australia). The dropshaft was 3.1 m high, 0.76 m wide and 0.75 long. The drop in invert was 1.7 m and the shaft pool was 1.0 m deep. The inflow and outflow channels were both horizontal, 0.5 m wide and 0.30 m deep. The upstream channel was open while the downstream conduit was covered and ended with a free overfall (Figs. 1 & 2).

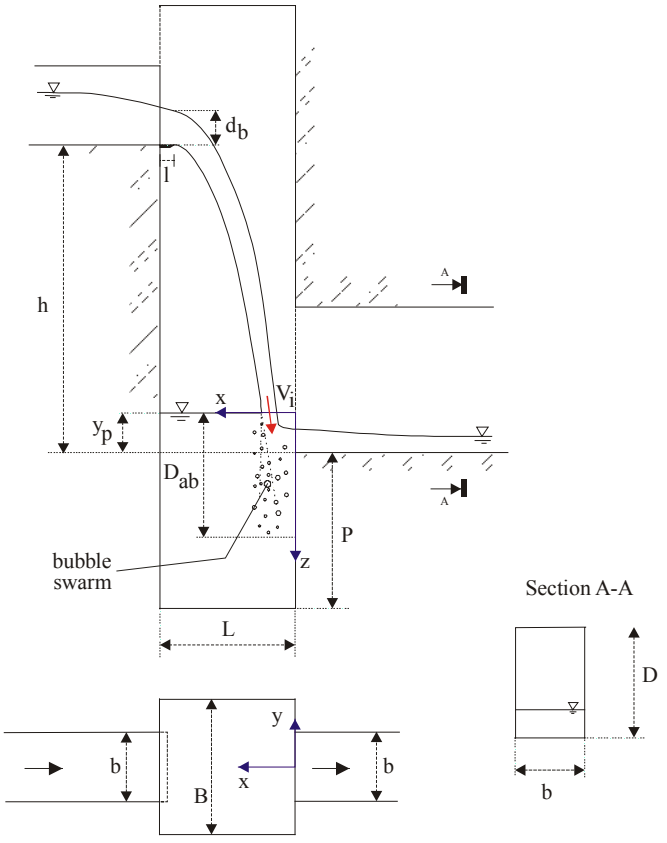

Fig.1 - Definition sketch of rectangular dropshafts

A flow rate of 12 L/s was used, for which the free-falling jet impacted into the shaft pool (Fig. 2), also called R1 regime [4]. Detailed air-water flow properties were measured with a single-tip conductivity probe (needle probe design). The probe consisted of a sharpened rod (platinum wire Ø=0.35 mm)

which was insulated except for its tip and set into a metal supporting tube (stainless steel surgical needle Ø=1.42 mm) acting as the second electrode. The probe was excited by an electronics designed with a response time less than 10 μs and calibrated with a square wave generator. During the present study, the probe output signal was scanned at 25 kHz for 100 seconds. Measurements were conducted at several cross-sections along the shaft centreline beneath the nappe impingement, with depths ranging from 0.03 m to 0.25 m (Table 1). The positions of the measurement points are listed in Table 1, where x is the horizontal distance measured from the downstream shaft wall and z is vertical direction positive downwards with z=0 at the pool free-surface.

Table 1 – Position of measurement points

Depth z - mm	x – mm
30	60-205
50	85-505
80	80-205
110	75-200
150	70-205
200	75-205
250	60-170

Fig.2 - Dropshat in operation with Q=12 L/s

The measurement principle of conductivity probes is based upon the difference in electrical resistivity between air and water. When the probe tip is in contact with an air bubble, the current between the tip and the supporting metal becomes zero. Although the signal is theoretically rectangular, the probe response is not square because of the finite size of the tip, the wetting/drying time of the interface covering the tip and the response time of the probe and electronics.

The data processing yielded the air concentration or void fraction C, the bubble count rate F and the bubble chord time t_{ch} [8]. The void fraction C is the proportion of time that the probe tip is in the air. Past experience showed that the probe orientation with the flow direction has little effect on the void fraction accuracy provided that the probe support does not affect the flow past the tip [9] [10]. In the present study, the probe tip was aligned with the flow direction. The bubble count rate F is the number of bubbles impacting the probe tip. The measurement is sensitive to the probe tip size, bubble sizes, velocity and discrimination technique, particularly when the sensor size is larger than the smallest bubble sizes. The bubble chord time t_{ch} is defined as the time spent by the bubble on the probe tip. The chord times were transformed into pseudo-bubble chord length ch_{ab} as:

$$ch_{ab} = V_i \, t_{ch} \quad (1)$$

where V_i is the jet impingement velocity [$L \cdot T^{-1}$] and t_{ch} is the measured bubble chord time [T]. Chanson et al. [10] compared Equation (1) with chord length measurements by Chanson & Brattberg [11] concluding that Equation (1) predicts the exact shape of bubble size probability distribution functions although it overestimates the bubble chord lengths by about 10 to 30%. The data accuracy is typically $\Delta C/C<2\%$ for void fractions between 0.03 to 0.95.

3 VOID FRACTION AND BUBBLE COUNT RATES. COMPARISON BETWEEN THEORETICAL TRAJECTORY OF THE FREE-FALLING NAPPE AND C_{MAX} DATA

Void fraction and bubble count rate data are discussed herein, while the region of maximum void fraction C_{max} is compared with theoretical underwater nappe trajectory location. The data are presented in terms of depth beneath the pool free-surface z, void fraction C and dimensionless bubble count rate $F \times d_c/V_c$, where d_c is the critical depth in the inflow channel [L] and V_c is the critical velocity [$L \cdot T^{-1}$], which is for a rectangular channel $V_c=(g \times d_c)^{0.5}$.

Figure 3a presents typical distribution of void fraction C along the dimensionless horizontal axis x/L for different depths, where x in the horizontal distance from the outer wall and L=0.755 m was dropshaft length (Fig. 1). Maximum value of C for each depth ranged from 0.60 down to 0.13 for $0.03 \leq z \leq 0.25$ m. Experimental results demonstrated very high void fraction next to the free-surface. Particularly, C values larger than 50% were observed at z=30 mm, z=50 mm and z=80 mm. Maximum void fraction was observed at z=50 mm. At z=110 mm and z=150 mm, maximum void fraction C were quite similar, i.e. 0.378 and 0.338, respectively. Finally, at z=200 mm and z=250 mm, C_{max} decreased down to 0.264 and to 0.133, respectively. The results were confirmed also by visual observation of the plunge region which demonstrated the boiling nature of the flow next to the impingement point. Visually, the plunge point area had the appearance of an "hydraulic jump roller". Further, the pool free-surface elevation fluctuated at low frequency with time.

Fig.3a - Void fraction C

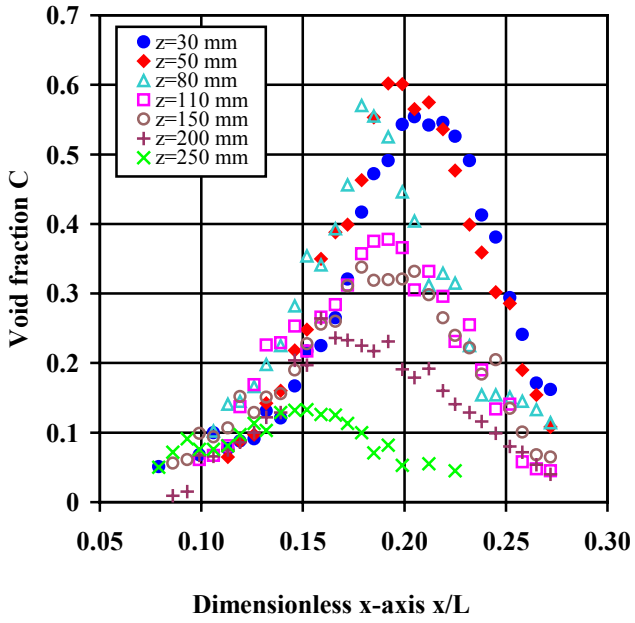

Overall, the measurements were performed in the fully developed flow region, i.e. $10 \leq z/d_i \leq 70$, except for the highest depth, i.e. z=30 mm, where z/d_i=7.23 and the flow is in the developing flow region. Notably, the nappe thickness d_i at the impact was calculated using Chanson's method [12] and it was found to be 0.004 m. In Figure 3a, note that the location of the maximum C value is shifted with increasing depth beneath the free surface toward the outflow, where x=0.

Void fraction data showed a quasi-exponential decay of maximum air content with longitudinal distance from the point of impingement and a broadening of the air diffusion layer. The data were successfully compared with the analytical solution of the diffusion equation for air bubble [13]:

$$C = \frac{1}{2}\,\frac{Q_{air}}{Q}\,\frac{1}{\sqrt{8\,\pi\,D^{\#}\,\frac{z}{d_i}}}\left(A_1 + A_2\right) \qquad (2)$$

where Q_{air} is the volume air flow rate, Q is the water discharge and D# is a dimensionless diffusivity which is equal to $D^{\#}=D_t/V_i \times d_i$, where D_t is turbulent diffusivity of air bubbles, $[L^2T^{-1}]$. Finally, A_1 and A_2 are:

$$A_1 = \exp\left[-\frac{1}{2\,D^{\#}}\,\frac{\left(\frac{x - x_i}{d_i} - \frac{1}{2}\right)^2}{\frac{z}{d_i}}\right] \qquad (3a)$$

$$A_2 = \exp\left[-\frac{1}{2\,D^{\#}}\,\frac{\left(\frac{x - x_i}{d_i} + \frac{1}{2}\right)^2}{\frac{z}{d_i}}\right] \qquad (3b)$$

where x_i is the x-location of the point of impact of the free-falling nappe. Visual observation revealed that the x-location of the point of impingement was about 0.155 m from the outflow channel. Equation (3) is favourably compared with the experimental data in Fig. 3b, where the full lines represent eq. (2) for z=30, 110 and 250 mm. The values of $D^{\#}$ and Q_{air}/Q ratio were determined from a best fit of the data. These values, together with z/d_i ratio values, are listed in Table 2. They are consistent with earlier values estimated in the same dropshaft with different flowrates [12] and also with vertical plunging jet results [13] [14].

Table 2 – Values of z/d_i, $D^{\#}$ and Q_{air}/Q ratio

Depth z - mm	z/d_i	Q_{air}/Q	$D^{\#}$
30	7.23	22.0	8.5
50	12.05	20.0	3.6
80	19.28	18.5	2.3
110	26.52	14.5	2.2
150	36.16	13.0	1.8
200	48.21	10.5	1.6
250	60.26	6.5	1.6

Fig.3b - Void fraction C and Eq. (2)

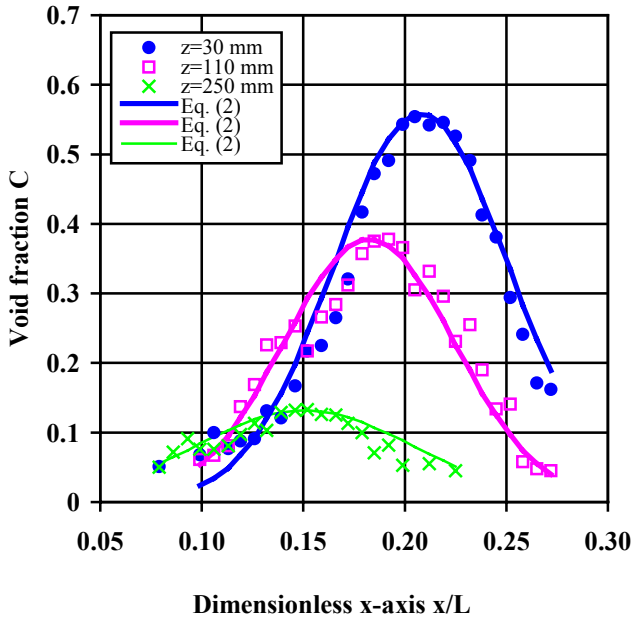

Figure 4 presents distribution of dimensionless bubble count rate $F \times d_c/V_c$ along the dimensionless horizontal axis x/L for different depths. For the investigations, i.e. Q=12 L/s, the critical velocity V_c and the critical depth d_c were 0.617 m/s and 0.0389 m, respectively. These distributions exhibit a marked peak and their maximum value ranged from 14.00 down to 4.82. In dimensional terms, the observed value of maximum bubble count rate were from 222 down to 77 Hz for $0.03 \leq z \leq 0.25$ m. Note also that the location of the maximum bubble count rate was shifted toward the outflow channel with increasing depths.

The trajectory of the underwater jet was calculated analytically using the approach of Chanson [6]. This analysis assumes that the velocity of the flow at the brink of the inflow conduit is nearly horizontal. Once the fluid leaves the canal edge, the horizontal acceleration is zero and the vertical

acceleration equals minus the gravity acceleration. For a two-dimensional nappe, the jet velocity components in the x- and z- directions are:

$$V_x = -V_b \quad (4a)$$

$$V_z = g\,t \quad (4b)$$

where V_b is the flow velocity at the brink of the step and t is the time. The trajectory equation of the nappe centreline is:

$$x = L - V_b\,t \quad (5a)$$

$$z = -\left(h - y_p + \frac{d_b}{2}\right) + \frac{1}{2}g\,t^2 \quad (5b)$$

where h is the drop height and d_b is the flow depth at the brink (Fig. 1). The brink velocity V_b and the brink depth d_b were 1.029 m/s and 0.023 m, respectively, while the free-surface height in the shaft pool above the downstream conduit invert y_p was measured as 0.058 m. Brink depth was calculated as $d_b=0.6\times d_c$ and, in turn, V_b was evaluated from the continuity with the critical condition. Note that Rouse equation, i.e. $d_b=0.715\times d_c$ [15], tended to underestimate brink velocity and to produce an x-location of the point of impingement that was too far from the outflow channel and was not consistent with visual observation. This is probably due to the non-zero vertical/downward velocity component at the brink, which is neglected in the calculations. Using $d_b=0.023$ m, the calculated x-location of the point of impingement was 0.157 from the downstream conduit and this value was consistent with visual observation. The nappe time to impact in the dropshaft was calculated as 0.58 seconds.

Fig.4 - Bubble count rate $F\times d_c/V_c$

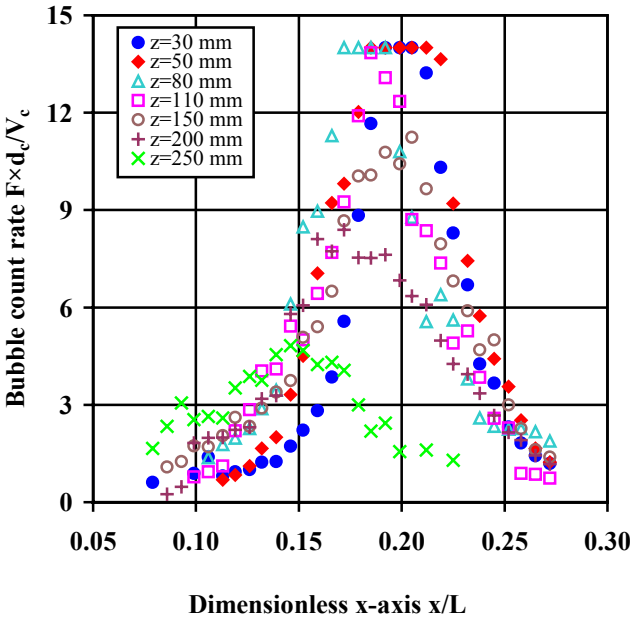

Fig. 5 presents the comparison of the calculated underwater jet trajectory with the x-locations of maximum void fractions, i.e. C_{max}, at each depth z. These points show a very close agreement, indicating that this trajectory is a good approximation of the underwater jet centreline.

Fig.5 - Nappe trajectory and C_{max}

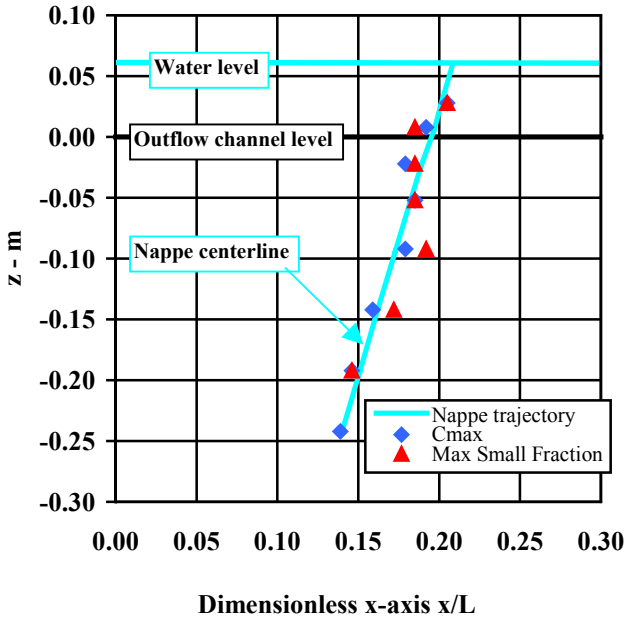

4 AIR BUBBLE CHORD LENGTH DATA. RESULTS. DISCUSSION

Instantaneous air and water chord times were recorded in the bubbly flow region of the shaft pool. The records were subsequently post-processed to study the air-water flow structure. Particularly, as previously outlined, bubble chord times t_{ch} were expressed in terms of pseudo-bubble chord length ch_{ab} using eq. (1). Chord length data were analysed and their main statistics, such as mean, median, mode, standard deviation, skewness and kurtosis, were estimated. The results for bubble chords ch_{ab} are given in Table 2, for each measurement depth and for x-locations closest to the jet trajectory, as derived in the previous section. Note that some data were highlighted in **bold**. Those data are the minimum values for that investigated depth. For example, at z=110 mm, the x-location closest to the jet trajectory had the minimum values for all the statistics.

Table 3 – Statistical properties of ch_{ab} next to the jet centreline

z - mm	x_t/L	Mean	Median	St. Dev.	Skewness	Kurtosis
30	0.201	**11.94**	**4.15**	21.21	4.07	24.72
50	0.196	12.42	4.61	21.48	3.89	20.63
80	0.189	12.17	4.61	21.26	4.27	26.55
110	0.182	**9.82**	**4.15**	**16.18**	**4.12**	**25.08**
150	0.173	13.03	5.30	24.52	5.65	48.92
200	0.162	11.84	5.07	20.50	4.57	29.44
250	0.150	10.37	**6.00**	14.32	6.38	86.12

The data in Table 3 demonstrate that the mean pseudo-bubble chord sizes were typically in the range from 9.8 to 13.0 mm. Also the basic statistics exhibit small variation along the jet trajectory at different depths.

Fig. 6 presents distribution of the mean air bubble chord length ch_{ab} along the dimensionless horizontal axis x/L for different depths. The data showed that the minimum mean

values were located about along the jet trajectory at each depth, where turbulent shear was maximum.

Fig.6 - Mean air chord length ch_{ab}

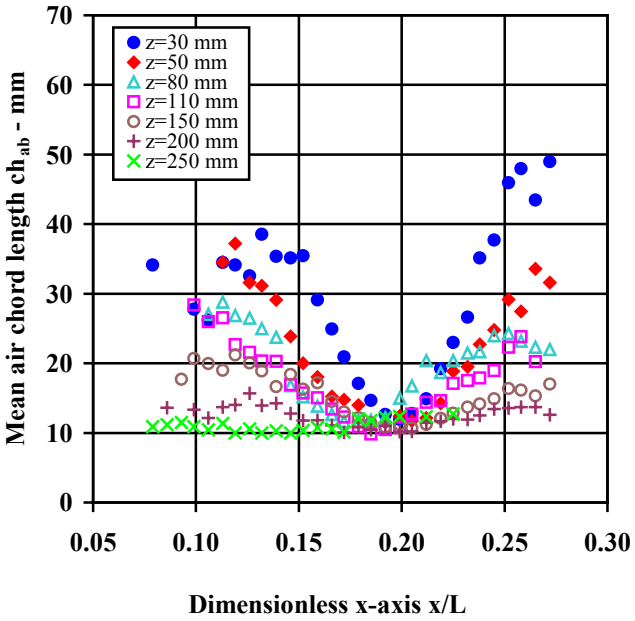

Table 4 lists the statistical properties in the x-location next to the jet trajectory at each depth also for the water chord length data ch_w. Minimum values for each depth are highlighted in bold. The data suggested a clear trend with the mean ch_w increasing with increasing depth. This result was confirmed also by median data. The trend is consistent with the decreasing number of air bubbles that can penetrate at increasing depth. Thus, as the mean size of the bubble is almost not changed, ch_w between two air bubbles increased.

Table 4 – Statistical properties of ch_w next to the jet centreline

z – mm	x_t/L	Mean	Median	St. Dev.	Skewness	Kurtosis
30	0.201	11.85	**5.54**	**16.66**	3.15	13.12
50	0.196	10.34	**4.84**	16.61	4.92	36.90
80	0.189	12.32	6.00	20.02	5.94	62.21
110	0.182	**16.40**	**7.38**	**26.65**	4.66	34.39
150	0.173	28.87	12.45	53.21	6.82	82.53
200	0.162	**32.95**	14.99	**54.26**	5.05	41.00
250	0.150	67.45	24.91	**134.49**	5.28	39.07

Air bubbles were further characterized using 3 fractions, namely small fraction (SF), medium fraction (MF) and big fraction (BF). The small fraction refers to air bubbles with ch_{ab} < 2.5 mm, the medium fraction to bubbles with 2.5 mm <ch_{ab} < 15 mm and the big fraction to the bubbles with ch_{ab} > 15 mm. These values were selected considering the typical ch_{ab} values observed in the pool. The big fraction is composed by large air packets which are subsequently broken up by turbulent shear. Thus, the small fraction represents the relative importance of the effect of this break-up process. In Fig. 5, the x-location of the points with maximum value of small fraction is presented. With increasing depth z beneath the free-surface, these locations tended to follow that of the jet trajectory. This trend confirms that fine bubble are produced in the jet flow as the results of break-up by turbulent shear.

Fig.7 - Small fraction PDF

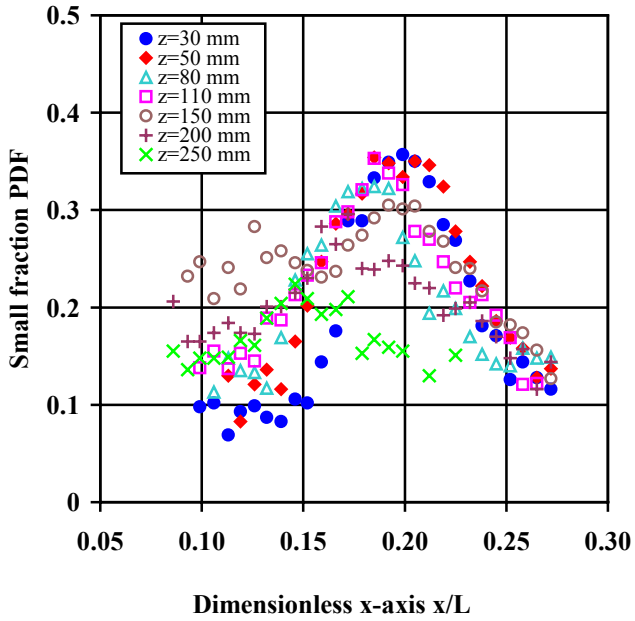

Fig. 7 presents the probability distribution function (PDF) of the SF at different depths. The data confirmed that the maximum numbers of small bubbles were observed next to the jet trajectory as already seen in Fig. 5. The data further demonstrated that the maximum value of the small fraction PDF decreased with the increasing depth. This is possibly caused by a combination of processes such as bubbles break-up by shear, bubbles coalescence and bubbles detrainment, i.e. the rise of some bubbles toward the free-surface of the pool.

Probability distribution functions (PDF) of air chord length were performed using 0.5 mm intervals. The data demonstrated the broad range of ch_{ab} values at each depth, with observed bubble sizes ranging from less than mm to more than 35 mm. The first class of the PDF was selected for ch_{ab} < 0.5 mm, whereas the last class was for ch_{ab} > 15 mm. Thus, 31 classes were considered. Fig. 8a presents the pseudo-bubble chord length PDF calculated for the x-position located next to the jet trajectory at z=30, 50 and 110 mm. The data showed always a large proportion of bubble chord greater than 15 mm. Also, the PDFs were skewed with a preponderance of small bubble sizes relative to the mean, which is illustrated in Table 3 by positive skewness. The probability of bubble chord length was the largest for bubble sizes between 0 and 2 mm, although the mean size was much larger.

The data for larger depths, i.e. z=150, 200 and 250 mm, are presented in Fig. 8b. At these depths, as for the earlier, the probability of bubble chord length was the largest for bubble sizes larger than 15 mm. Then, at these 3 depths the PDF shape was different as the class n.6, i.e. 2.5 < ch_{ab} <3.0 mm, had PDF value higher than those with lower ch_{ab} values. Also, the probability of the smaller fraction decreased with the increasing depth. This trend could be again explained as due to a combination of processes previously outlined such as bubbles coalescence and detrainment. Notably, the PDF shape for z=110 mm represents a transition from those of lower

depths and those of higher depths.

Fig.8a - Bubble chord length ch_{ab} PDF

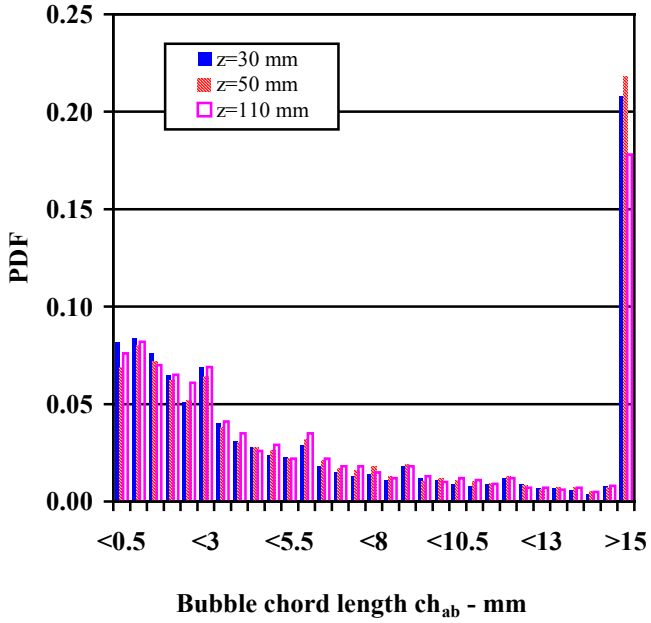

Fig.8b - Bubble chord length ch_{ab} PDF

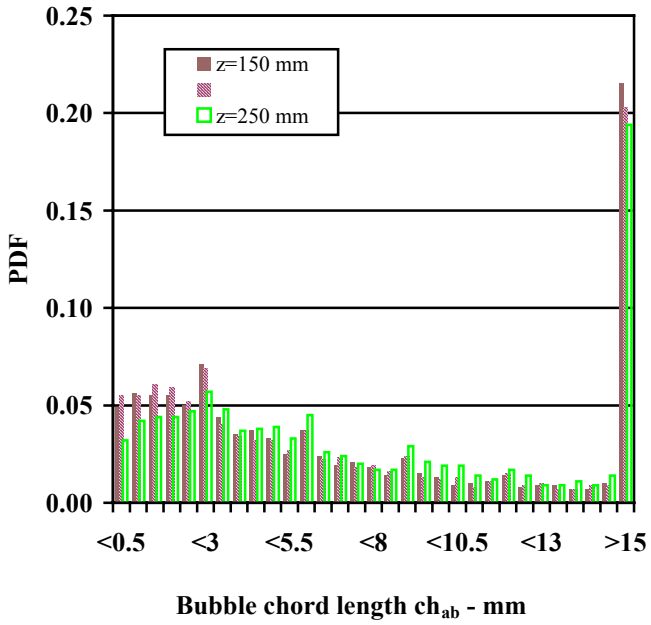

Overall the results highlighted that the mean pseudo-chord sizes were in the range from 9 to 13 mm. The chord size distribution data suggested that there was a significant number of large entrained air packets at each of the considered depths. This result was consistent with experimental measurements in the developing region of vertical plunging jets [10] [14]. Finally, it is believed that bubbles coalescence and detrainment processes tended to reduce the percentage of the smaller air bubbles along the jet trajectory with increasing depth.

5 COMPARISON WITH DATA FOR DIFFERENT FLOWRATES. DISCUSSION

In this section, the results previously presented are compared with those obtained with different flowrates. These results were presented in [11], where the considered flowrates were Q=7.6, 16 and 67 L/s. The first two flowrates belonged to the R1 regime, whereas for Q=67 L/s, the free-falling jet impacted to the downstream wall, also called R3 regime [4]. In the following comparison only data for Q=7.6 and 16 L/s were considered.

Fig.9a - C for Q=7.6, 12 and 16 L/S

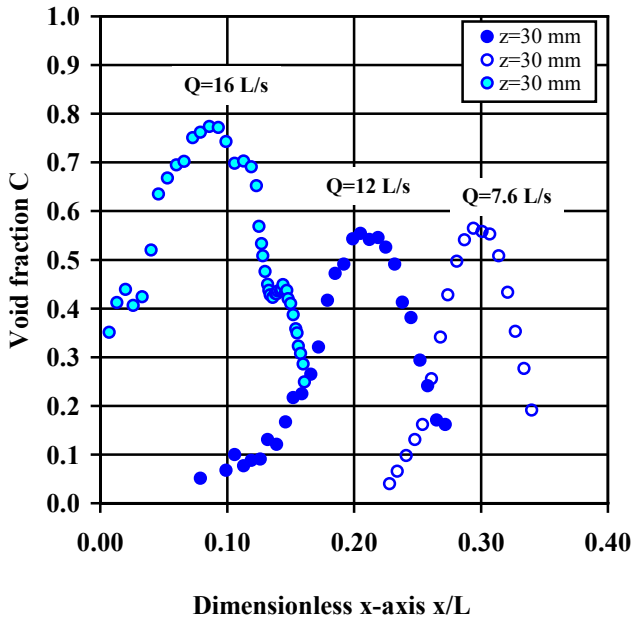

Fig.9b - C for Q=7.6, 12 and 16 L/S

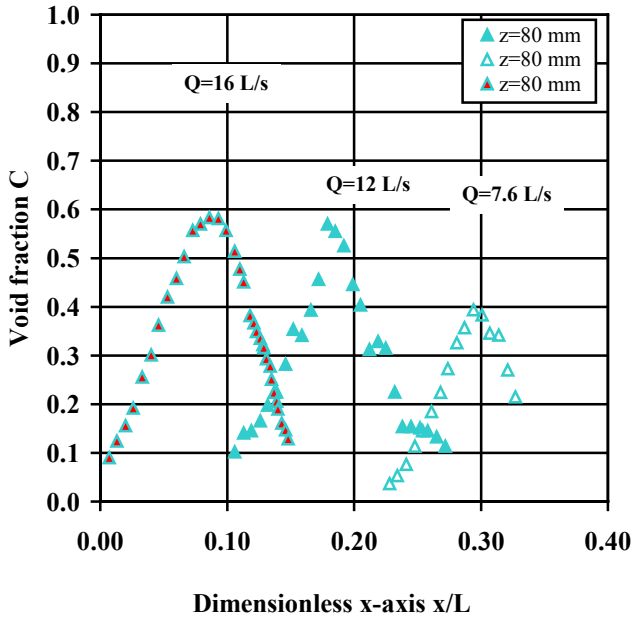

First of all, void fraction C data and dimensionless bubble count rate $F \times d_c/V_c$ were compared. Figs. 9a. 9b & 9c present void fraction distributions at different depths. Fig. 9a present C data at z=30 and Fig. 9b shows data at z=80 mm. The data for Q=7.6 L/s are the empty circles and triangles, while the data for Q=12 L/s are the full circles and triangles. Finally,

data for Q=16 L/s are the circles and the triangles on the left.

The shape of the graphs was the same for all the depths and the flowrates, but they were shifted along the dimensionless horizontal axis x/L because the point of impingement tended to be shifted towards to the downstream conduit with the increasing flowrate. At z=30 mm maximum values of C were similar for Q=7.6 L/s and Q=12 L/s, as they were 0.565 and 0.554, respectively, whereas C_{max} for Q=16 L/s was higher than the earlier, i.e. 0.774. Only at z=80 mm, there was a trend with C_{max} which increased with the increasing flowrate. In fact, C_{max} was 0.394, 0.570 and 0.583 for Q=7.6, 12 and 16 L/s, respectively. Fig. 9c presents void fraction data at z=150 and 250 mm. The data for Q=7.6 L/s are the empty squares, whereas data for Q=12 L/s are the full squares and the product symbols. Finally, data for 16 L/s are the squares on the left and the small horizontal line. Data for Q=7.6 L/s and z=250 mm were not available. The void fraction values were generally lower than those at higher depths. At z=150 mm, C_{max} values for Q=7.6 L/s were significantly lower than those for the higher flowrates.

Overall, the analysis of C data for different flowrate does not support a trend between C_{max} and the flowrate.

Fig.9c - C for Q=7.6, 12 and 16 L/S

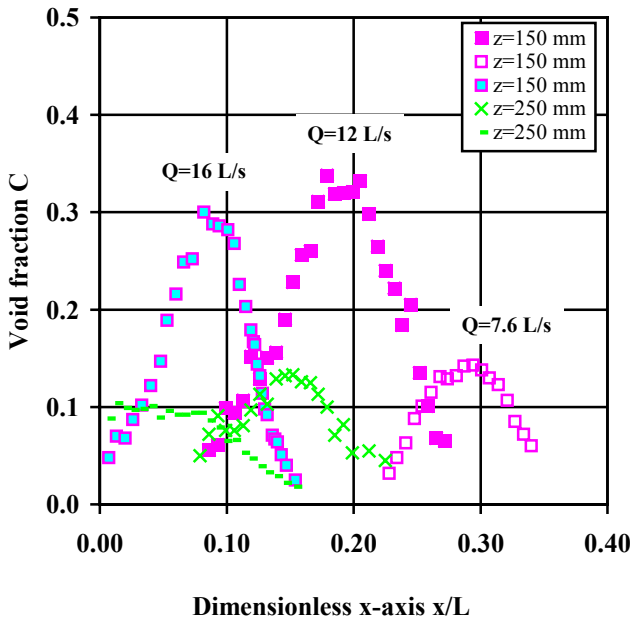

Figs. 10a & 10b presents dimensionless bubble count rate $F \times d_c/V_c$ data. The symbols used in the figures are the same used for the void fraction. Fig. 10a shows $F \times d_c/V_c$ data for z=30 and 80 mm. Also $F \times d_c/V_c$ graphs were shifted along the dimensionless horizontal axis x/L to x/L=0 with the increasing flowrate. At z=30 mm, data for Q=12 L/s were higher than those for the other flowrates. Also, for Q=7.6 and 12 L/s, there was no significant difference between values at z=30 mm and z=80 mm. For Q=16 L/s, dimensionless bubble count rate $F \times d_c/V_c$ data have higher values for z=80 mm than for z=30 mm. Particularly, the maximum value is similar to that for Q=12 L/s. Fig. 10b presents $F \times d_c/V_c$ data for z=150 and 250 mm. At z=150 mm, the maximum values for Q=12 and 16 L/s were similar and higher than that for Q=7.6 L/s. At z=250 mm, maximum values for Q=12 and 16 L/s were also similar.

Fig.10a - $F \times d_c/V_c$ for Q=7.6, 12, 16 L/s

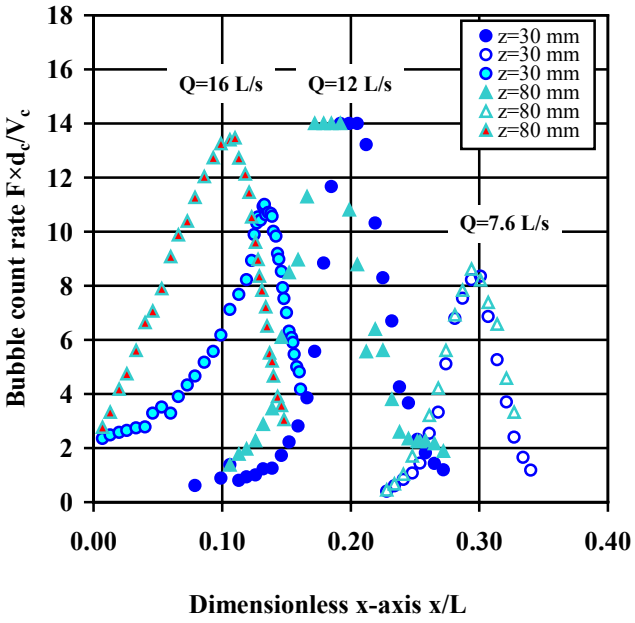

Fig.10b - $F \times d_c/V_c$ for Q=7.6, 12, 16 L/s

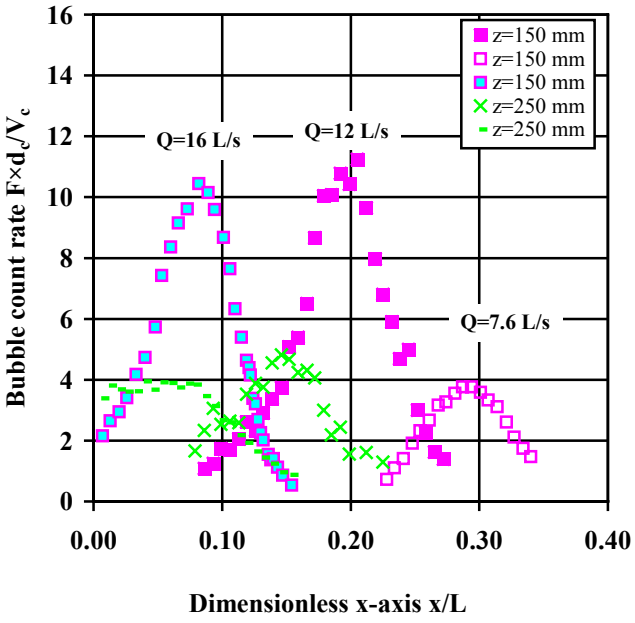

6 CONCLUDING REMARKS

This study presents new experimental results obtained in a large-size rectangular dropshaft structure. The facility was a nearly full-scale shaft comparable to sewer structures and stormwater systems. That is, these results are little affected by scale effects.

The results demonstrated a strong aeration of the shaft pool with void fraction C values up to 60% and larger than 50% at z=30 mm, z=50 mm and z=80 mm. Theoretical trajectory calculations of the free-falling nappe were favourably compared with visual observations and show that the data with maximum void fraction C_{max} were located on the jet centreline. Also, void fraction C data were successfully compared with an analytical solution of diffusion equation for air bubbles [13].

The analysis of the air bubble pseudo-chord data highlighted that mean sizes were in the range from 9 to 13 mm. Also, at each depth, minimum mean values were located about along the jet trajectory, where turbulent shear was maximum. Water chord data confirmed that a decreasing number of air bubbles could penetrate at increasing depths. The air chord size distribution data suggested that there was a significant number of large entrained air packets at each of the considered depths. Furthermore, the data confirmed that bubble coalescence and detrainment processes reduced the percentage of the smaller air bubbles along the trajectory with increasing depth.

A comparison of void fraction C data and dimensionless bubble count rate $F \times d_c/V_c$ data with those previously obtained with different flowrates, does not support a trend between maximum void fraction C_{max} and flowrate.

Finally, the results obtained were very useful as design tool in order to use the dropshaft as flow reaeration structure. In fact, the presented results complete the characterization of the air-water flow properties of the dropshafts.

Acknowledgment

The experimental works described in this paper have been conducted when the first author was *Visiting Scholar* at the Department of Civil Engineering of The University of Queensland. The first author acknowledges that his Scolarship was funded by the Exchange Program for Professors and Researchers of the University of Napoli *Federico II* for the year 2003 and wishes to thank Prof.Guido Trombetti, Magnifico Rettore of the University of Napoli *Federico II*.

Symbols

C = air concentration, also called void fraction;
C_{max} = maximum air concentration in the air bubble diffusion layer;
ch_{ab} = pseudo-bubble chord length;
ch_w = pseudo-water chord length;
D_t = turbulent diffusivity of air bubbles;
$D^{\#}$ = dimensionless turbulent diffusivity of air bubbles;
d_b = brink depth, i.e. depth at the edge of the drop;
d_c = critical flow depth in the inflow channel;
d_i = nappe thickness at the impact;
F = air bubble count rate;
g = gravity constant. g = 9.80 m/s² in Brisbane;
h = drop in invert elevation;
L = dropshaft length;
Q = flowrate of water;
Q_{air} = volume air flow rate;
t = time;
t_{ch} = bubble chord time;
V_b = brink flow velocity;
V_c = critical flow velocity;
V_i = impingement velocity of the nappe;
x = horizontal distance measured from the downstream shaft wall;
x_i = horizontal distance of the point of impact of the nappe;
x_t = horizontal distance of the jet trajectory;
y = transverse distance measured from the shaft centreline;
y_p = free-surface height in a shaft pool above the downstream conduit invert;
z = vertical distance from the pool free-surface, positive downwards;

References

[1] Merlein, J., Kleinschroth, A. & Valentin, F., Systematisierung von Absturzbauwerken. *Mitterilung No. 69*, Lehrstuhls fur Hydrauli und Gewasserkunde, Technishen Universitat Munchen, Germany, 206 pages, 2002

[2] Apelt, C.J., Goonyella Railway Duplication Drop Structures and Energy Dissipators at Culvert Outlets. Model Studies. *Report CH27/84*, Dept. of Civil Engineering, University of Queensland, Australia, Feb., 10 pages, 11 figures & 37 plates, 1984

[3] Vischer, D. & Hager, W.H., *Dam Hydraulics,* John Wiley, Chichester, UK, 316 pages, 1998

[4] Chanson, H., An Experimental Study of Roman Dropshaft Hydraulics, *Jl of Hyd. Res.*, IAHR, **40**, No.1, pp.3-12, 2002

[5] Rajaratnam, N., Mainali, A. & Hsung, C.Y., Observations on Flow in Vertical Dropshafts in Urban Drainage Systems, *Jl of Environmental Engrg.*, ASCE, **123**, No.5, pp.486-491, 1997

[6] Chanson, H., The Hydraulics of Roman Aqueducts: Steep Chutes, Cascades and Dropshafts *Research Report No. CE156*, Dept. of Civil Engineering, University of Queensland, Australia, 97 pages, 1998

[7] Gualtieri C. & Chanson H., Clustering process and interfacial area analysis in a large-size dropshaft., *5th International Conference on Advances in Fluid Mechanics (AFM 2004)*, Lisbon, Portugal, March 22-24, 2004

[8] Chanson, H., Air-Water Flow Measurements with Intrusive Phase-Detection Probes. Can we Improve their Interpretation ?, *Jl of Hyd. Engrg.*, ASCE, Vol. 128, No. 3, pp. 252-255, 2002

[9] Chanson H., A Study of Air Entrainment and Aeration Devices on a Spillway Model, *Ph.D. thesis*, Ref. 88-8, Dept. of Civil Engrg., University of Canterbury, New Zealand, 1988

[10] Chanson, H., Aoki, S. & Hoque, A., Similitude of Air Bubble Entrainment and Dispersion in Vertical Circular Plunging Jet Flows. An Experimental Study with Freshwater, Salty Freshwater and Seawater, *Coastal/Ocean Engineering Report*, No. COE02-1, Dept. of Architecture and Civil Eng., Toyohashi University of Technology, Japan, 94 pages, 2002

[11] Chanson H. & Brattberg T., Air-Water Bubbly Flow in Free-Shear Layers *Proc.1996 ASME Fluids Eng. Conf.*, San Diego, USA, ASME-FED Vol. 236, Vol.1, pp. 357-364, 1996

[12] Chanson, H., An experimental study of roman dropshaft operation: hydraulics two-phase flow, acoustics, *Research Report No. CE50/02*, Dept. of Civil Engineering, University of Queensland, Australia, 2002

[13] Cummings P.D. & Chanson H., Air entrainment in the developing region of plunging jets. Part 1: Theoretical development, *Journal of Fluids Engineering,* Trans, ASME, vol.119, n.3, pp. 597-602, 1997

[14] Cummings P.D. & Chanson H., Air entrainment in the developing region of plunging jets. Part 2: Experimental, *Journal of Fluids Engineering,* Trans, ASME, vol.119, n.3, pp. 603-608, 1997

[15] Rouse H., Fluid Mechanics for Hydraulic Engineers. McGraw-Hill, New York, USA, 1938